Cryo-EM structure of the bacteria killing type IV secretion system core complex from *Xanthomonas citri*

Germán G. Sgro[#,1,2], **Tiago R. D. Costa**[#,2,a], **William Cenens**[1], **Diorge P. Souza**[1,b], **Alexandre Cassago**[3], **Luciana C. Oliveira**[1,c], **Roberto K. Salinas**[1], **Rodrigo V. Portugal**[3], **Chuck S. Farah**[1,*], and **Gabriel Waksman**[2,4,*]

[1]Departamento de Bioquímica, Instituto de Química, Universidade de São Paulo, Av. Prof. Lineu Prestes 748, CEP 05508-000, São Paulo, SP, Brazil

[2]Institute of Structural and Molecular Biology at UCL and Birkbeck College, Department of Biological Sciences, Birkbeck College, Malet Street, WC1E 7HX, London, United Kingdom

[3]Laboratório Nacional de Nanotecnologia (LNNano), Centro Nacional de Pesquisa em Energia e Materiais (CNPEM), CEP 13083-970, Campinas, SP, Brazil

[4]Institute of Structural and Molecular Biology at UCL and Birkbeck College, Research Department of Structural and Molecular Biology, Division of Biosciences, University College London, WC1E 6BT, London, United Kingdom

[#] These authors contributed equally to this work.

Abstract

Type IV secretion (T4S) systems form the most common and versatile class of secretion systems in bacteria, capable of injecting both proteins and DNAs into host cells. T4S systems are typically composed of 12 components that form two major assemblies: the inner membrane complex embedded in the inner membrane and the core complex embedded in both the inner and outer

[*]**Correspondence and requests for materials** should be addressed to C.S.F. (chsfarah@iq.usp.br) or G.W. (g.waksman@mail.cryst.bbk.ac.uk).
[a]Present address: MRC Centre for Molecular Bacteriology and Infection, Department of Life Sciences, Imperial College London, SW7 2AZ, London, United Kingdom.
[b]Present address: MRC Laboratory for Molecular Cell Biology, University College London, WC1E 6BT, London, United Kingdom.
[c]Present address: Department of Pathology and Cell Biology, Institute for Research in Immunology and Cancer, Université de Montréal, H3T 1J4, Québec, Canada.

membranes. Here we present the 3.3 Å resolution cryo-electron microscopy model of the T4S system core complex from *Xanthomonas citri*, a phytopathogen that utilizes this system to kill bacterial competitors. An extensive mutational investigation was performed to probe the vast network of protein-protein interactions in this 1.13 MDa assembly. This structure expands our knowledge of the molecular details of T4S system organization, assembly and evolution.

Type IV secretion systems are ubiquitous nanomachines used by bacteria and archaea to mediate transfer of a large variety of DNAs and proteins into prokaryotic and eukaryotic targets. They mediate bacterial conjugation, and so are essential drivers in the spread of antibiotic resistance genes. In their role as virulence factors in pathogenicity, they secrete transforming DNAs into plants to cause tumorigenic growths[1] and also effector proteins into animal cells to cause widespread infectious diseases[2–7]. More recently, it was shown that the phytopathogen *Xanthomonas citri* utilizes its T4S system to secrete effectors that are lethal to other bacterial species, thus placing these systems as major fitness determinants of interspecies bacterial competition[8,9].

Canonical T4S systems have 12 conserved subunits termed VirB1-11 and VirD4[1,10]. They can be structurally divided into two subcomplexes, a circa 2.5 MDa inner membrane complex and a circa 1 MDa core complex[11–13] (Supplementary Fig. 1a). The core complex of canonical T4S systems is composed of 14 copies each of VirB7, VirB9 and VirB10 proteins with most of its mass located within the bacterial periplasm, but also embedded in both the inner and outer membranes (IM and OM, respectively) via N- and C-terminal transmembrane helices of the VirB10 protein[14]. The core complex architecture consists of two ringed layers, the O- and I-layers (Supplementary Fig. 1a)[14]. The O-layer is associated with the OM through a cap which forms a channel composed of 14 two-helix bundles contributed by the C-terminal domain of VirB10 (VirB10$_{CTD}$)[15]. This OM channel is buttressed just under the OM by a ring formed by VirB10$_{CTD}$ on the inside and the C-terminal domain of VirB9 (VirB9$_{CTD}$) on the outside[15]. In canonical T4S systems, the small (circa 30-40 residue) VirB7 lipoprotein subunits lay on the outer surface of VirB9 covalently attached to a lipid moiety in the inner leaflet of the OM. Under the O-layer, lies the I-layer formed by the N-terminal domains of VirB9 and VirB10 (VirB9$_{NTD}$ and VirB10$_{NTD}$, respectively; Supplementary Fig. 1b)[14]. To date, the only atomic resolution information available for T4S systems is the circa 0.6 MDa structure of the core complex O-layer from the conjugative plasmid pKM101[15], formed by TraN/VirB7, TraO$_{CTD}$/VirB9$_{CTD}$ and TraF$_{CTD}$/VirB10$_{CTD}$. The atomic resolution structure of the circa 0.5 MDa I-layer remains unknown.

Here we present the structure of a 1.13 MDa core complex made of the full-length VirB7, VirB9, and VirB10 proteins from *X. citri*, solved by cryo-electron microscopy at 3.3 Å resolution. This structure provides the first atomic resolution model of the I-layer as well as that of an O-layer that includes an extra VirB7 globular domain that has intriguing similarities with features observed in other pathogenic T4S systems. The roles of specific structural features in the *in vivo* stabilization of the T4S system and in mediating the killing of bacterial rivals by *X. citri* were investigated.

Results

General architecture of the *X. citri* T4S system core complex

The *X. citri* VirB7, VirB9 and VirB10 proteins were overexpressed and purified from *E. coli* (Fig. 1a). A cryo-EM data set of approximately 185,000 particles (Fig. 1b, Supplementary Table 1) was used to compute an electron density map with an average resolution of 3.3 Å and a local resolution extending to 3.1 Å (Fig. 1c,d, Supplementary Fig. 1c-e). Top/bottom view class averages clearly indicated an overall 14-fold symmetry (Fig. 1c). This 1.13 MDa core complex resembles a flying saucer decorated with 14 lateral "pods" each made of the C-terminal domain of the VirB7 subunit (Fig. 2a,b, Supplementary Fig. 1b). An atomic model with excellent stereochemistry and fit to the density could be built and refined (Fig. 1e, Supplementary Table 1), encompassing VirB7 residues 22-132, VirB9 residues 27-141 and 148-255 and VirB10 residues 150-161, 183-323 and 339-389 (Fig. 1f). The 182 N-terminal residues of VirB10 were mostly disordered, which is not unexpected considering that residues 84-184 between the inner membrane spanning helix and the globular VirB10$_{CTD}$ is rich in proline residues (Supplementary Fig. 2).

Fourteen heterotrimers (labeled -6 to +7 in a clockwise manner) assemble to form the core complex (Fig. 2a). Each heterotrimer can be divided into a central compact core region (made up of the N-terminal region of VirB7, the VirB9$_{CTD}$ and the VirB10$_{CTD}$), and the more detached VirB9$_{NTD}$ and the C-terminal "N0" domain of VirB7, both connected to the central core by extended linkers (Figs. 2c-e, 3b). The compact core region, including the rest of VirB7, form the O-layer of the core complex while the VirB9$_{NTD}$s and the mostly disordered VirB10$_{NTD}$s form the I-layer (Fig. 2c).

The *X. citri* O-layer

The *X. citri* O-layer (minus the VirB7 N0 domains) is homologous to that of pKM10115 (overall root-mean-square deviation (RMSD) of 2.6 Å; Fig. 3c, Supplementary Fig. 3), as is the nature of most of the intermolecular contacts and the contact surface areas between the 3 proteins in this region (reported in Supplementary Table 2 for *X. citri*). A detailed comparison of the O-layers in these two structures is presented in Supplementary Figure 3.

An important feature of the *X. citri* core complex O-layer is the globular C-terminal N0 domain[16] of VirB7 (residues 54-132) composed of two central α-helices flanked on one side by a 3-stranded β-sheet and on the other by a 2-stranded β-sheet and a small 3_{10} helix (Figs. 3, 4c). Seen from above, these N0 domains wrap clockwise around the outer perimeter of the O-layer (Fig. 2a), as previously predicted[16], the result being that while the N-terminal sequence of VirB7 (residue 22 to 38) interacts primarily with the VirB9$_{CTD}$ of the same heterotrimer (Supplementary Fig. 4a), the N0 domain interacts with both the VirB9$_{CTD}$ and the VirB7 linker (residues 39 to 53) from an adjacent heterotrimer (Figs. 2a, 4c and Supplementary Fig. 4c). In this latter VirB7-VirB7 interface, residues 45 to 49 form a small β-strand (β2) that pairs with strand β5 of the N0 domain from the neighboring VirB7 subunit (as previously observed[16]).

The atomic structure of the I-layer

Another significant feature presented here is the atomic resolution structure of the I-layer. Most of the observed density in this region is derived from the 14 VirB9$_{NTD}$s, each of which exhibits a β-sandwich fold made of 5-stranded and 4-stranded β-sheets, with one α-helix (α1) lying under the β-sandwich in a loop between β-strands 8 and 9 (Figs. 3b, 4d). VirB9$_{NTD}$s interact extensively with each other (Fig. 4a,d, Supplementary Fig. 4d) to form the I-layer ring with an internal diameter of 80 Å at its base (Fig. 2c). The VirB9$_{NTD}$-VirB9$_{NTD}$ interface (720 Å^2) (Supplementary Table 2) arises from the juxtaposition of the 4-stranded β-sheet of one VirB9$_{NTD}$ with the 5-standed β-sheet of its neighbor and possesses many of the features of an intramolecular β-sandwich with a central hydrophobic core decorated by interactions between polar residues (Supplementary Fig. 4d). Notably, the VirB9$_{NTD}$ β-sandwiches make few, if any, stereospecific contacts with the O-layer, with important implications for models of T4S system function (see below).

The VirB9$_{NTD}$ is expected to interact with at least part of the VirB10$_{NTD}$ in the I-layer[17], though specific details regarding this interaction are not yet available. While most of the VirB10$_{NTD}$ seems to be disordered in the present structure, we observed some significant electron density at the base of the I-layer between adjacent VirB9$_{NTD}$ domains (Fig. 4f). This patch of isolated electron density was of sufficiently high resolution that it could be traced and built as a 12-residue α-helix. To test whether this density might correspond to a structured region of the VirB10$_{NTD}$, we expressed and purified ^{13}C/^{15}N-labeled VirB10$_{NTD}$ (residues 85-182) and unlabeled VirB9$_{NTD}$ (residues 27-150) for NMR-based interaction studies, as described in detail in Supplementary Figure 5 and Supplementary Table 3. These NMR studies, in conjunction with the side chain pattern of residues in the electron density map, led us to assign the density of the α-helix in the I-layer region to the sequence P$_{150}$TLLERRILAES$_{161}$ of VirB10$_{NTD}$ (Fig. 4f). Hereafter, this helix will be referred to as the VirB10$_{NTD\_150\text{-}161}$ helix.

Disordered VirB9 and VirB10 linkers and absence of stereospecific contacts between the O- and I-layers

Long linkers between domains in all three proteins project part of their structure away from the heterotrimeric central core region in the O-layer (Fig. 2). Of particular interest are the linkers that join the NTDs and CTDs of the VirB9 and VirB10 subunits between the I- and O-layers, respectively. In the case of VirB9, a long linker (residues 131 to 161) emerges from the VirB9$_{NTD}$ β-sandwich and meanders to the VirB9$_{CTD}$ ~37 Å away in a clockwise (+) direction (Fig. 3a,b). This linker is partially disordered, with a 15-Å stretch corresponding to residues 142-147 that could not be traced, but has one notable structural feature, α-helix 2 (α2), that is involved in numerous interactions with adjacent and non-adjacent heterotrimers in the O-layer (specifically VirB10$_{CTD}$ of heterotrimers -1 and -2; Fig. 4e, Supplementary Fig. 4e) but very few, if any, contacts within the I-layer.

In the case of VirB10, the first secondary structure element in the O-layer, β1 (residues 185-191), extends in a counterclockwise (-) direction and inserts itself between the β-strands β11 and β17 at the base of the β-barrel of VirB10$_{CTD}$ in the adjacent heterotrimer (Fig. 4b, Supplementary Fig. 4b). This interaction is similar to that observed in the pKM101 O-layer

for the β-strand in the so-called "lever arm" that precedes the $TraF_{CTD}$/$VirB10_{CTD}$15. In this structure, the lever arms extend horizontally for 55 Å in the plane of the O-layer, making contacts with the lever arms of adjacent subunits as well as with the $VirB10_{CTD}$s up to three subunits away15. However, in the *X. citri* core complex, no density was observed for the residues corresponding to the α-helix and unstructured region of the pKM101 lever arm.

At least 40 Å separates the last residue of the $VirB10_{NTD\_150-161}$ helix at the base of the I-layer and the first visible residue in $VirB10_{CTD}$ (Gly183) at the base of the O-layer (the distance may be greater depending on which $VirB10_{CTD}$/$VirB10_{NTD\_150-161}$ helix pair is chosen, as depicted in Supplementary Figure 6a) and the vector connecting these two points is roughly orthogonal to the VirB10 lever arm in the pKM101 O-layer structure15. This puts restrictions on the secondary structure and direction to be adopted by the intervening 21-residue sequence between the $VirB10_{NTD\_150-161}$ helix and $VirB10_{CTD}$ (Supplementary Fig. 6a).

Functional analysis of structural features of the *Xanthomonas* core complex

In vivo assays of T4S system assembly and function—Figure 5a (left panel) shows the time course of a colorimetric bacterial killing assay in which the rate of chlorophenol red-β-D-galactopyranoside (CPRG) cleavage is proportional to the number of *E. coli* cells that have been lysed by *X. citri* in a T4S system-dependent manner (see Methods for details). Interestingly, *X. citri virB10-msfGFP* cells, in which the *virB10* gene was substituted with a chimeric gene that codes for VirB10 and monomeric superfolder green fluorescent protein (msfGFP) fused to its C-terminus, is capable of killing *E. coli* cells in these competition assays with an efficiency approximately 81% that of wild-type *X. citri* cells (Figs. 5a, 6a, Supplementary Table 4). Furthermore, microscopy analysis shows that these *X. citri virB10-msfGFP* cells have distinct fluorescent foci in the bacterial periplasm (Figs. 5a, 6a, Supplementary Table 4). On the other hand, *X. citri virB10-msfgfp* cells in which the *virB7* gene was deleted are not able to kill *E. coli* and do not present periplasmic foci (Fig. 5b). We therefore decided to use this *X. citri virB10-msfGFP* strain as a reference in experiments designed to test the effect of mutations on the assembly of a stable core complex in the *X. citri* periplasm. Several experimental controls that were performed to validate the use of the *X. citri virB10-msfGFP* strain are described in detail in Supplementary Note and Supplementary Figure 7. Thirty four specific point mutations in the chromosomal copies of the *virB7*, *virB9* or *virB10* genes were produced in one or both of two different genetic backgrounds: i) wild-type *X. citri* (27 of 34 mutations) and/or ii) the *X. citri virB10-msfGFP* strain (33 of 34 mutations) (Supplementary Table 4). Figure 5b presents the fluorescence images and real-time killing assay curves of several representative mutants and the data obtained for all the mutants (in both backgrounds) is summarized in Figure 6, Supplementary Table 4 and Supplementary Figure 7. The fluorescence microscopy images of hundreds to thousands of cells from each strain were analyzed in order to obtain a distribution of the number of fluorescent foci per cell (Fig. 6a, Supplementary Table 4). Below, we describe the phenotypes of these mutants in the context of their perturbations of specific structural features of the *X. citri* core complex.

VirB7-VirB9 and VirB7-VirB7 interactions—Three VirB7 residues, Asn38, Val37 and Trp34, shown here to interact with VirB9$_{CTD}$ of the same heterotrimer (Supplementary Fig. 4a) and shown previously to reduce the strength of the VirB9-VirB7 interaction with increasing degrees of severity *in vitro* (N38A<V37G<W34A)9 also presented the same order in severity of loss of T4S system function in the *E. coli* lysis assay with N38A, V37G, and W34A mutants (Figs. 5, 6, Supplementary Table 4). Deletion of the whole N0 domain (by introducing a stop codon at position 39 of the *virB7* gene) abolished T4S system-dependent killing in both backgrounds. Though the VirB7 N0 domain is positioned very close to the VirB9$_{CTD}$ of neighboring heterotrimer +1 (Supplementary Fig. 4c), very few stereospecific contacts are observed and thus, it is not surprising that mutation of interface residues Met60 in the VirB7 N0 domain or the simultaneous mutation of Ile157 and Lys159 in the VirB9$_{CTD}$ resulted in moderate reductions in killing activity in the VirB10-msfGFP background and very little change in the non-GFP background (Supplementary Table 4). Mutations in the VirB7 linker (F40A and I47A/P48A/L49A) that mediates VirB7-VirB7 interactions caused more significant reductions in bacterial killing efficiency in the VirB10-msfGFP background but very little change when introduced into the non-GFP background (Figs. 5, 6, Supplementary Table 4). These results suggest that the VirB10-msfGFP chimera potentiates the destabilizing effects of mutations in the VirB7-VirB9 and VirB7-VirB7 interfaces, possibly because msfGFP attachment to the VirB10 C-terminus places it just below the interface between the VirB9$_{CTD}$ and VirB7 N0 domains.

VirB10$_{CTD}$-VirB10$_{CTD}$ and VirB9$_{CTD}$-VirB10$_{CTD}$ interactions in the O-layer—The large interface between VirB10$_{CTD}$s has a notably high number of hydrophilic side chains between neighboring β-barrels. For example, a cluster of acidic and basic residues forms an intricate network of salt bridges: Arg200 and Asp380 from one subunit and Asp263, Arg264 and Asp272 from the subunit in heterotrimer +1 (Supplementary Fig. 4b). Disruption of this network of ionic interactions by introducing substitutions in VirB10 residues Arg264 or Asp380 drastically reduce T4S system-mediated bacterial killing efficiency in both non-GFP and VirB10-msfGFP backgrounds with a concomitant total absence of fluorescent foci (Fig. 6a, Supplementary Table 4). Another set of salt bridges is made between VirB10 residues Arg211 and Asp281 and VirB9$_{CTD}$ Glu216 from the preceding heterotrimer (Supplementary Fig. 6b). Disruption of these interactions by mutating Arg211 to glutamate in the VirB10-msfGFP background only moderately reduces killing activity and the mean number of foci (Supplementary Table 4). Finally, we probed another three-way interaction involving the intramolecular salt bridge formed by residues Arg205 and Glu226 in the VirB10$_{CTD}$ which also H-bond to the side chains or backbone carbonyl groups from residues Thr201, Tyr235 and Leu219 in VirB9$_{CTD}$s from the same heterotrimer and heterotrimer -1 (Supplementary Fig. 6b). Mutating VirB10 residue Arg205 to alanine significantly reduces (but does not abolish) foci formation and abolishes killing in the VirB10-msfGFP background but, surprisingly, has no effect on bacterial killing efficiency in the non-GFP background. The reason for this discrepancy may be related to the fact that Arg205 is located in β3 that pairs with β16 just before the VirB10 C-terminus (Fig. 1f). Mutation of VirB10 Glu226 in the VirB10-msfGFP background had a more moderate effect while the double R205A/E226A mutant abolishes foci formation and killing. (Fig. 6a, Supplementary Table 4). Taken together, these results suggest that ionic interactions at the VirB10$_{CTD}$-VirB10$_{CTD}$ interface

are more important for T4S stability and function than those encountered at the VirB10$_{CTD}$-VirB9$_{CTD}$ interface.

Mutation of Cys206 in the well-conserved intramolecular disulfide bond with Cys222 in the VirB10$_{CTD}$ (Supplementary Fig. 4b) results in abolition of T4S system function in both VirB10-msfGFP and non-GFP backgrounds (Fig. 6a, Supplementary Table 4). This mutation seems to be particularly disruptive since microscopy analysis of *X. citri* VirB10$_{C206S}$-msfGFP cells presented no periplasmic foci and very little background fluorescence (Fig. 5b, Supplementary Table 4, Supplementary Fig. 7). In fact, the only other VirB9 or VirB10 mutants to present significantly reduced periplasmic fluorescence are also mutations in the VirB10$_{CTD}$ (R264D, D380A, R264D/D380R and R205A/E226A discussed above; Supplementary Table 4, Supplementary Fig. 7).

VirB9$_{NTD}$-VirB9$_{NTD}$ and VirB9$_{NTD}$-VirB10$_{NTD}$ interactions in the I-layer—The homotropic interactions involving adjacent VirB9$_{NTD}$ domains make a major contribution to the stability of the core complex I-layer. These intermolecular interactions involve hydrophobic patches, one of which is made up of residues Val28, Val29, Ile39, Ile103, Tyr126 and Val129 (Supplementary Fig. 4d). We made a series of single, double and triple mutations in residues Val29, Ile103 and Tyr126 in the non-GFP and VirB10-msfGFP backgrounds and all displayed a severely reduced or total lack of T4S system-dependent killing (Fig. 6a, Supplementary Table 4). Another highly buried residue in this interface is Tyr81 (Supplementary Fig. 4d) and its mutation to alanine or glutamic acid resulted in moderate to severe reductions in T4S system function in both non-GFP and VirB10-msfGFP backgrounds (Fig. 6a, Supplementary Table 4).

The only stereospecific interaction that we detected between the VirB10$_{NTD}$ and VirB9$_{NTD}$ was that of the VirB10$_{NTD\_150-161}$ helix that fits into a groove between two neighboring VirB9$_{NTD}$s (Fig. 4f). Residues Phe67 and Asp88 from one VirB9 subunit and Trp113 from VirB9 of the neighboring heterotrimer (+1) take part in these interactions with Arg155 and Arg156 from the VirB10$_{NTD\_150-161}$ helix. Mutating these residues in both VirB10-msfGFP and non-GFP backgrounds results in moderate to significant reductions in killing efficiency (Fig. 6, Supplementary Table 4). Therefore the specific VirB9$_{NTD}$-VirB9$_{NTD}$ and Vir9$_{NTD}$-VirB10$_{NTD\_150-161}$ helix interactions that maintain the I-layer intact play a major role in T4S system function. The difficulty our group and others have encountered attempting to study VirB9$_{NTD}$-VirB10$_{NTD}$ interactions using isolated domains may be in large part due to the entropic barrier that inhibits formation of this three-way interaction in solution which is overcome in the context of the tetradecameric complex

The linkers between NTDs and CTDs of VirB9 and VirB10 and the I-layer/O-layer interface—The presence of long linkers between domains appears to be a recurring theme in T4S system core complex structures. The length of the linker between VirB9$_{NTD}$ and VirB9$_{CTD}$ is reasonably well conserved (Supplementary Fig. 2b). Within this linker, helix α2 is particularly interesting as it sits at the interface between two VirB10$_{CTD}$ subunits of heterotrimers -1 and -2 in the O-layer but makes no non-covalent contacts with VirB9$_{NTD}$s in the I-layer. In the case of VirB10, the last residue of the VirB10$_{NTD\_150-161}$ helix and the first visible residue at the base of the O-layer are separated by at least 40 Å

(Supplementary Fig. 6a). Specific mutants were produced to probe the importance of these linkers that connect VirB9 and VirB10 NTDs and CTDs in the two layers. Interestingly, deletion of the disordered residues lacking electron density (Ala142-Ser147) immediately following VirB9 α2 had no effect on bacterial killing or formation of fluorescent foci (Fig. 6, Supplementary Table 4). Also, the simultaneous mutation of two VirB9 α2 residues (S137A/F138A) within the interface with the O-layer (Supplementary Fig. 4e) had only a negligible effect on bacterial killing activity (Fig. 6, Supplementary Table 4). Finally, deletion of 8 residues (Gln175-Asp182) from the disordered region between the VirB10$_{NTD\_150-161}$ helix and the base of the O-layer, only moderately reduced T4S system-mediated killing in the VirB10-msfGFP background and had no significant effect on killing in the non-GFP background (Fig. 6, Supplementary Table 4), an observation consistent with the only moderate phenotype observed for a deletion in the lever arm of TraF/VirB10 from pKM10118. Together, these results suggest that the transmission of information between the O- and I-layers may not pass through the covalent linkages connecting the two layers.

The pore in the outer membrane formed by the VirB10 antennae—In both the *X. citri* and pKM101 core complex structures, the fourteen VirB10 α1/α2 helix pairs come together to form a diaphragm-like pore in the outer membrane (Fig. 4a, Supplementary Fig. 3). In the *X. citri* structure, the cryo-EM map shows no density for VirB10 residues 324-337 (sequence: TTTIGVGSGIVTQQ; Supplementary Fig. 2c) in the extracellular loop between α1 and α2. Deletion of a major portion of this loop (residues 325-335) in the VirB10-msfGFP background produced only a moderate reduction in foci formation and killing efficiency (Fig. 6a, Supplementary Table 4). This implies that either the core complex can undergo a major conformational change to further close the pore or the pore is naturally gated by other components of the T4S system (for example VirB2 or VirB5). We note that similar deletions in the *E. coli* pKM101 Tra and *Agrobacterium tumefaciens* VirB/VirD4 systems retained partial function in DNA transfer assays18.

Discussion

This 3.3 Å resolution structure of the *X. citri* T4S system core complex provides the first atomic resolution model of an I-layer containing VirB9$_{NTD}$s and their specific interactions with a helical region of the VirB10$_{NTD}$, as well as the detailed structure of an expanded O-layer containing VirB7 N0 domains. Mutations that interfere with the extensive, highly stereospecific interfaces that maintain the O- and I-layers intact, characterized by deeply buried hydrophobic residues and intricate networks of ionic interactions produced strong defects in T4S system assembly and function as did mutations that interfered in the less extensive VirB9$_{NTD}$-VirB10$_{NTD\_150-161}$ helix contacts. Very few stereospecific interactions are observed between the O-layer and I-layer and between the VirB9$_{CTD}$s and peripheral VirB7 N0 domains within the O-layer, which explains why mutations at these interfaces produce only moderate effects.

The linkers between the VirB9 and VirB10 NTDs and CTDs could, if they were conformationally rigid, impose restrictions on the relative orientations between subunits in the I- and O-layer. The observations that reducing their lengths had only moderate effects on T4S system function reinforces the hypothesis that flexibility is an intrinsic property of these

linkers15 and that the contacts between I- and O-layers and contacts between VirB9$_{NTD}$s and VirB10$_{NTD}$s within the I-layer are both weak and malleable. This opens up the prospect that the layers could in fact experiment multiple relative orientations of one ring with respect to the other in terms of rotation and/or dissociation at different stages of the substrate translocation process.

The disposition of VirB7 N0 domains on the outer periphery of the O-layer provides a detailed view of functionally important and intriguing structural variability within the canonical group of T4S systems. There is, in fact, a large amount of sequence and size diversity in proteins annotated as VirB7 in the protein sequence databases, but their C-terminal extensions have no apparent sequence similarity to the N0 domain sequences found in Xanthomonadaceae VirB7 proteins. We have previously pointed out the topological similarities between *X. citri* VirB7 and *L. pneumophila* DotD proteins16. Interestingly we were able to find a low amount of sequence similarity between *X. citri* VirB7 and the N-terminal half of the *H. pylori* CagT protein and, as described in Supplementary Discussion and Supplementary Figure 8, the disposition of VirB7 N0 domains on the peripheral surface of the *X. citri* core complex may be analogous, if not homologous, to the spokes that decorate the inner ring of the *H. pylori* Cag T4S system.

The clear correlation between the number of fluorescent foci and the killing activity of the mutants in the VirB10-msfGFP background (Fig. 6a) was surprising since we had expected to isolate at least a few mutants which were able to assemble (i.e. present near wild-type levels of foci) but were non-functional. In hindsight, this may be because the mutants were designed to disrupt subunit-subunit interactions. Future studies could test other mutants in the channel lumen expected not to affect the core complex stability but rather perturb weaker or transient interactions with other T4S system components or with substrates during translocation.

Methods

Cloning, expression and purification of the T4S system core complex of *X. citri*

The sequence coding for the *virB7*, *virB8*, *virB9* and *virB10* genes in the *X. citri* genome was amplified by PCR as a single fragment using oligonucleotides containing NdeI and NotI restriction sites (Supplementary Table 5). The PCR fragment was then introduced into the pET-24a-based pGGS2a vector, designed to add a C-terminal Strep-tag and created using specific primers (Supplementary Table 5) and the QuikChange II site-directed mutagenesis kit (Agilent), cut using the same restriction enzymes. T4 DNA ligase was used to yield the plasmid pGGS2a:*virB7-virB10*$_{C-Strep}$, which was transformed into BL21(DE3) strain. Protein overexpression was induced by addition of 0.25 mM of IPTG during the exponential growth phase for 18 hours at 18 ºC. After this time, cells were harvested by centrifugation at 8,000 x g for 20 minutes. Crude membrane fraction was isolated by ultracentrifugation (120,000 x g for 1 hour) after cells were broken using an EmulsiFlex-C5 system (Avestin) and a low-speed centrifugation step (15,000 x g for 30 minutes). Membrane proteins were then solubilized overnight with mild agitation in 50 mM Tris-HCl (pH 8.0), 100 mM NaCl, 1 mM EDTA, 0.8% LDAO (Anatrace) and 1% DDM (Anatrace), and insoluble material was removed by centrifugation (100,000 x g for 40 minutes). The detergent-solubilized protein

fraction was loaded onto a Strep-Tactin sepharose affinity column (GE Healthcare). The column was washed with 50 mM Tris-HCl (pH 8.0), 150 mM NaCl, 10 mM LDAO and eluted in the same buffer supplemented with 10 mM d-Desthiobiotin (Sigma-Aldrich). Eluted proteins were then concentrated by filtration using a 100-kDa cut-off spin concentrator and loaded onto a HiLoad Superose 6 GL 16/700 gel filtration column (GE Healthcare) equilibrated in 20 mM Tris-HCl (pH 8.0), 200 mM NaCl, 10 mM LDAO. Protein content was analyzed by SDS-PAGE and Coomassie Blue staining and concentration determined using the bicinchoninic acid (BCA) method (Sigma).

Expression and purification of VirB9$_{NTD}$ and VirB10$_{NTD}$

Recombinant *X. citri* VirB9$_{NTD}$ was expressed in *E. coli* BL21(DE3) RP cells harboring the plasmid pET28a-*virB9$_{XAC2620}$*_27-150, in which the VirB9$_{NTD}$ (residues 27 to 150) coding sequence was cloned between the NdeI and BamHI restriction sites (Supplementary Table 5). Expression of VirB9$_{NTD}$ was induced in a culture (OD$_{600}$=0.8) grown in 2xTY medium at 25 ℃ by the addition of 0.4 mM of IPTG. After eight hours, cells were collected by centrifugation, resuspended in 20 mM Tris-HCl (pH 8.0), 200 mM NaCl, 20 mM imidazole, and lysed using a French Press. The lysate was clarified by centrifugation at 27,000 x g at 4 ℃ for 40 minutes. The supernatant was applied onto a Ni^{2+}-HiTrap column (GE Healthcare) equilibrated with 20 mM Tris-HCl (pH 8.0), 200 mM NaCl, 20 mM imidazole and eluted using a linear 20-500 mM imidazole gradient over 20 column volumes. Fractions containing VirB9$_{NTD}$ were pooled and applied onto a HiLoad Superdex 75 26/600 column (GE Healthcare) equilibrated with 20 mM Tris-HCl (pH 8.0), 100 mM NaCl. After size exclusion separation, buffer exchange to 20 mM sodium acetate (pH 5.5), 150 mM NaCl was performed during concentration to 270 μM using a spin concentrator.

The DNA sequence encoding VirB10$_{NTD}$ (residues 85 to 182) was chemically synthetized with codon optimization for expression in *E. coli* and cloned into the expression vector pET28a between NdeI and BamHI restriction sites (GenScript). Uniformly ^{15}N/^{13}C doubled labeled His-VirB10$_{NTD}$ was expressed in *E. coli* BL21(DE3) RP cells in M9 minimal medium containing 1.0 g/L of ^{15}NH$_4$Cl and 2.0 g/L of ^{13}C-glucose as the only nitrogen and carbon sources, respectively. Expression of His-VirB10$_{NTD}$ was carried out at 37 ℃ for 7 hours upon the addition of 0.5 mM IPTG when the bacterial culture reached OD$_{600}$ = 0.4. Cells were harvested, resuspended in 20 mM Tris-HCl (pH 8.0), 200 mM NaCl, and lysed using a French Press. The lysate was centrifuged at 27,000 x g at 4 ℃ for 40 minutes and the supernatant was loaded onto a Ni^{2+}-HiTrap column (GE Healthcare) equilibrated with 20 mM Tris-HCl (pH 8.0), 200 mM NaCl and 10 mM imidazole and eluted with an imidazole gradient as described above. Fractions containing His-VirB10$_{NTD}$ were combined and dialyzed against 10 mM Tris-HCl (pH 7.5), 150 mM NaCl overnight at 4 ℃. The His-tag was removed by incubation with thrombin-agarose resin (Sigma-Aldrich) for 5 hours at 25 ℃ and subsequent size exclusion separation and buffer exchange to 20 mM sodium acetate (pH 5.5), 150 mM NaCl using a Hiload 26/600 Superdex 75 column (GE Healthcare). The fractions were collected and concentrated to 300 μM by filtration using a 3-kDa cut-off spin concentrator after which 0.05% NaN$_3$ and 10% D$_2$O were added. Where indicated, a VirB10$_{NTD}$:VirB9$_{NTD}$ (1:1.8) mixture was made by adding 500 μL of 270 μM unlabeled

VirB9$_{NTD}$ to 500 µL of 150 µM ^{13}C-^{15}N-VirB10$_{NTD}$, followed by concentration to a final volume of 500 µL.

Electron microscopy sample preparation and data collection

To evaluate the quality and homogeneity of the *X. citri* core complex purifications, aliquots (~3 µL) were applied onto glow-discharged, carbon-coated copper grids (Agar Scientific). After incubating the sample for ~2 minutes at room temperature, the grids were rapidly washed with three successive drops of deionized water and then exposed to a solution of 2% uranyl acetate. Images were recorded on either a JEOL JEM 2100 microscope (operating at 200 kV) or a Philips Tecnai T12 microscope (operating at 120 kV), both using a LaB$_6$ filament and coupled to a charge-coupled device (CCD). For cryo-EM sample preparation, aliquots (~4 µL) of purified *X. citri* core complex at a concentration of ~0.3 mg/mL were deposited onto glow-discharged ultra-thin carbon film on Lacey 400 mesh copper grids (Agar Scientific). A Vitrobot Mark IV (FEI) plunge-freezing device operating at 22 ºC and 100% humidity was used to incubate the sample with the grid for 30 seconds and blot for 4.5 seconds prior to vitrification in liquid ethane. The data were collected at the eBIC facility at the Diamond synchrotron using a FEI Titan Krios transmission electron microscope, operated at 300 kV and equipped with an energy filter (Gatan GIF Quantum, USA). Dataset (1,469 micrographs) were automatically acquired with EPU software (FEI), recorded on a K2 Summit direct electron detector (Gatan) operated in super-resolution counting mode with a physical pixel size of 1.06 Å/pixel (0.53 Å per super-resolution pixel). The detector was placed at the end of a GIF Quantum energy filter operated in zero-energy-loss mode with a slit width of 20 eV. The total exposure time was 12 seconds and intermediate frames were recorded every 0.3 seconds giving an accumulated dose of ~60 e$^-$/Å^2 and a total of 40 frames per image. The defocus range used for data collection was ~1.0 µm to ~3.0 µm.

Cryo-EM image processing and reconstruction

All micrographs were first subjected to patch-based motion correction using MotionCor2[19], with two-fold binning (1.06 Å/pixel after binning) and dose-weighting. The contrast transfer function parameters of the corrected micrographs were determined using the Gctf software[20]. After screening the micrographs for poor Thon rings or resolution estimation over 3.6 Å, 1,390 micrographs remained for further processing. Unless otherwise stated, RELION 2.0[21] was used for all subsequent processing steps. Approximately 4,000 particles were manually picked from selected micrographs to generate representative 2D class averages. These classes were used as templates for automated particle picking for the entire dataset. A total of 185,079 particles were auto-picked and extracted using a box size of 350x350 pixels. Several rounds of reference-free 2D classification were performed and 142,306 particles were kept in good class averages. All particles were then subjected to 3D classification with the CryoSparc software[22] generating one good 3D map with 99% of the particles. This map was then low-pass filtered to 50 Å and used as a reference for 3D auto-refinement with imposed C14 symmetry. In subsequent steps, a solvent mask and a B-factor of -138 was applied improving the overall resolution of the map to 3.28 Å assessed by the gold standard criterion (FSC-0.143), implemented in RELION 2.0. Local resolution estimations in the map were performed with RELION 2.0.

Model building and refinement

The electron density was clearly interpretable which allowed us to build a *de novo* structural model. This process began by fitting the crystallographic model of the *X. citri* VirB7 C-terminal N0 domain (PDB:3OV5)16 and the NMR model of the *X. citri* VirB9$_{CTD}$-VirB7$_{NTD}$ complex (PDB:2N01)9 in order to identify the map with the correct handedness. Models were positioned using "Fit in map" tool in Chimera23, and saved relative to the map. Using these as starting points, we were able to manually build the rest of the model for VirB7 and VirB9$_{CTD}$, and the *de novo* models for VirB10$_{CTD}$, VirB10$_{NTD\_150-161}$ and VirB9$_{NTD}$ using Coot24. In this manner, we obtained a combined model for a single VirB7-VirB9-VirB10 heterotrimer unit, which was submitted to iterative rounds of real space refinement and building using PHENIX25 and Coot software, respectively. Thirteen more copies of the refined heterotrimer were then fit into the density map using Chimera23 and new rounds of real space refinement (now using NCS for the 42 chains contained in the structure) and building using PHENIX and Coot, respectively, were executed until we obtained good parameters for Ramachandran plot and MolProbity26. Chimera23 and PyMol27 were used for map and model visualization and figure production.

NMR spectroscopy

NMR spectra were acquired at 280 K on a Bruker Avance III spectrometer operating at 800 MHz (1H frequency) and equipped with a cryogenic TCI probe. Backbone resonances assignments were obtained from the analysis of a set of standard triple-resonance NMR experiments28: HNCA, HN(CO)CA, HNCACB, CBCA(CO)NH, HNCO and HN(CA)CO. NMR spectra were processed with NMRPipe29 and analyzed using CCP_NMR Analysis 2.4.130. The backbone resonances were used as input for the prediction of secondary structure propensity using SSP31 and of backbone dihedral angles (Φ and Ψ) using TalosN32. The heteronuclear $\{^1H\}$-^{15}N-NOE experiment was performed in interleaved fashion using saturation time and inter-scan relaxation delay of 3 seconds. The heteronuclear NOE values were obtained from the cross peak intensity ratios of spectra recorded starting from the pure ^{15}N polarization with or without presaturation of the ^{1}H spins.

Engineering *X. citri* genome by two-step allelic exchange

All modifications in *X. citri* genomic DNA were introduced by two-step allelic exchange. Briefly, *X. citri* strain 306 cells34 (see below for specific mutants) were electroporated with 2 μg of plasmid DNA at 200 Ω, 25 μF and 2 kV using a Gene Pulser II with the Pulse Controller II and Capacitance extender II modules (Bio Rad). The first allelic exchange was selected by plating cells on 15-cm diameter LB-agar plates supplemented with Kanamycin (Km) 50 μg/mL at 30 ºC for 2-3 days. Colonies on these plates have integrated the plasmid into the chromosome by homologous recombination either using the up- or downstream 1000-bp fragments cloned in pNPTS138 for this purpose. Hereafter, a group of Km-resistant colonies were picked and streaked directly onto NaCl-free LB-Agar plates supplemented with sucrose (10 g/L tryptone, 5 g/L yeast extract, 60 g/L sucrose and 15 g/L agar), selecting for cells that recently excised the integrated pNPTS138 plasmid by a second homologous recombination between the duplicated 1000-bp up, or downstream, merodiploid regions. Several single colonies were scored for loss of Km resistance and finally for presence of

either the desired or wild-type DNA version by PCR, using primers annealing outside the cloned region and confirmed by Sanger sequencing of the PCR product.

Construction of the *X. citri virB10-msfgfp* strain

The *msfgfp* gene was amplified from pDHL102933, introducing a flexible N-terminal linker (SGGGG). Separately, ~1000 bp of the upstream and downstream regions from the stop codon of *virB10* were amplified by PCR (Phusion polymerase, Thermo Scientific) from *X. citri* strain 30634 genomic DNA, using primers containing either homology to the pNPTS138 vector (Km[R], *sacB*, ColE1 ori)8 backbone or the *msfgfp* gene (Supplementary Table 5). The three fragments were cloned into the pNPTS138 vector using Gibson Assembly (NEB), thereby creating a seamless inserting of msfGFP with a linker just before the native *virB10* stop codon35. This vector, pNPTS138:*virB10-msfgfp*, was transformed in *X. citri* wild-type strain using the protocol described above in order to obtain the *X. citri virB10-msfgfp* strain.

Construction of *X. citri* mutant strains

Due to the high number of different mutants to be tested in the components of the core complex of *X. citri*, we decided to group them based on their vicinity in the genome. For VirB7, all mutations (W34A, V37G, N38A, F40A, I47A/P48A/L49A, N0 and M60A) were included in one single group; for VirB9, mutations V29D, I103D, Y126D, F67R, D88R, Y81A, Y81E and W113A were included in group A, mutations S137A, F138A, A142-S147, I157A and K159A in group B, and mutation R250A in group C; for VirB10, mutations R155A, R156A and Q175-D182 were included in group A, mutations C206S, R211E, R205A, E226A in group B, and mutations R264D and D380R in group C. Thus, for each group there was created a pNPTS138-based plasmid containing ~1000 bp upstream and downstream from the nucleotide located at the center of the respective group, by PCR using specific primers for each case (In-Fusion® HD Cloning System, Clontech, Supplementary Table 5) and genomic DNA from the *X. citri* strain 306 (wild-type) or *X. citri virB10-msfgfp* strain, as previously described. All of the mutations (single, double, triple and deletions) were introduced into the corresponding pNPTS138-derived vector by PCR and self-ligation using specific primers for each case (In-Fusion® HD Cloning System, Clontech, Supplementary Table 5). Note that in some cases (combinations of mutations V29D, I103D, Y126D and F67R/D88R in VirB9, and R205A/E226A and R264D/D380R in VirB10) two or three rounds of mutagenesis were required to introduce changes in sites too far apart to be changed simultaneously with a single pair of primers.

Chlorophenol red-β-D-galactopyranoside (CPRG) bacterial competition assay

To visualize and quantify the ability of *X. citri* to lyse *E. coli* strain MG1655 cells, a CPRG-based method36 was used with some adaptations. When CPRG (yellow) is cleaved by LacZ it forms a red-colored diffusible product that can be easily detected with a plate-reader at 572 nm. Importantly, CPRG is not able to penetrate bacterial cells and will only be cleaved by extracellular LacZ. As such, the rate of CPRG cleavage is proportional to the number of *E. coli* cells that have lysed (X. citri strain 306 lacks an active *lacZ* gene). To each well of a clear U-shaped bottom 96-well plate (Greiner), 100 μL of a mixture of 0.5X buffer A (0.1% $(NH_4)_2SO_4$, 0.3% Na_2HPO_4, 0.15% KH_2PO_4, 0.15% NaCl)37, 1.5% agarose and 40 μg/mL

CPRG (Sigma-Aldrich) was added, and plates were thoroughly dried under a laminar flow. *X. citri* cells were grown overnight in 96 well plates in AB medium (0.2% $(NH_4)_2SO_4$, 0.6% Na_2HPO_4, 0.3% KH_2PO_4, 0.3% NaCl, 0.1 mM $CaCl_2$, 1 mM $MgCl_2$, 3 μM $FeCl_3$)[37] supplemented with 0.2% sucrose, 0.2% casamino acids, 10 μg/mL thiamine and 25 μg/mL uracil. After determination of the optical density of the culture of each *X. citri* stain (normally between 0.6 and 0.8), they were mixed in a 1:1 volume ratio with an *E. coli* culture that had been grown to $OD_{600}=1$ in the presence of 0.2 mM IPTG, washed once and concentrated 10 times. Five microliters of these mixtures were immediately added to the 96-well plate without puncturing or damaging the agarose, covered with a transparent seal and quickly thereafter absorbance at 572 nm (A_{572}) was monitored in a 96-well plate reader for at least 200 minutes (SpectraMax Paradigm, Molecular Devices). Note that in order to yield consistent results for this assay, plates must be very dry so that the 5-μL mixtures are absorbed within minutes. Mutants were organized in 96-well plates together with both *X. citri*, *X. citri virB10-msfGFP* and *E. coli* controls. Assays were performed 3 or 4 times for each mutant, 9 times for *X. citri virB10-msfGFP* and 27 times for wild-type *X. citri*, and the averages of the resulting killing curves are presented with their standard deviations. To control for putative secondary modifications in the mutant's genetic background beyond the targeted *loci*, wild-type revertant strains obtained during the selection of each mutant were all confirmed to have wild-type killing efficiencies. The A_{572} values were processed using RStudio software[38] and plotted using the ggplot2 package[39]. Background intensities obtained from the mean of A_{572} values of two repeats containing only *E. coli* cells were subtracted from the data series. Hereafter, each series was normalized to the initial OD_{600} values from each *X. citri* culture to correct for small differences in OD_{600} after overnight growth (Note that no significant difference in growth rate could be detected for the mutants, except for mutant VirB10 $_{Q175-D182}$ which also showed smaller cell sizes). Next, the initial A_{572} value at time-point 0 minutes was subtracted from all subsequent time-points to correct for small differences in initial A_{572} measurements. Finally, each set of mutants was normalized to their wild-type counterparts, leading to the final figures shown with $A_{572}=0$ serving as the *E. coli* control baseline. Additionally, to produce a single numerical comparison of the data, the mean slope (obtained by calculating the discrete first derivative) between time-point 50 and 100 minutes of the obtained normalized A_{572} curves of mutant and wild-type cells were compared to obtain the fraction of killing efficiency of each mutant compared to the wild-type *X. citri virB10-msfGFP* control (killing efficiency set to 1.0; Figs. 5, 6 and Supplementary Table 4). These calculations did not in any way distort the conclusions initially drawn based on the analysis of the raw data.

Fluorescence microscopy image acquisition and analysis

To analyze the distribution of msfGFP-labeled VirB10 in the *X. citri* periplasm with mutant and wild-type *virB* loci, cells were grown in the same conditions as for the CPRG-competition assays described above. Briefly, 1 μL of cell suspension was spotted on a thin agarose slab containing 1X buffer A (0.2% $(NH_4)_2SO_4$, 0.6% Na_2HPO_4, 0.3% KH_2PO_4, 0.3% NaCl)[37] and 2% agarose and covered with a #1.5 cover glass (Corning). Phase contrast and msfGFP emission images were obtained with a Leica DMI-8 epifluorescent microscope. msfGFP emissions were captured using a 1500 ms exposure time at maximum excitation light intensities. The microscope was equipped with a DFC365 FX camera

(Leica), a HC PL APO 100x/1.4 Oil ph3 objective (Leica) and a GFP excitation-emission band-pass filter cube (Ex.: 470/40, DC: 495, Em.: 525/50; Leica). In order to increase spatial resolution, eleven 0.05 μm Z-plane stacks were obtained from a 0.5 μm region within the center of the cells. This allowed for a better signal to noise ratio of the VirB10-msfGFP foci and increased detection of VirB10-msfGFP foci location in different depths of the cell. These image stacks were background subtracted by a rolling ball correction using a significant cell-free portion of each image as a reference and, finally, combined by an average intensity projection using the FIJI software package40. To obtain a quantitative representation of the amount of foci present per cell, the images were analyzed using the MicrobeJ software package41, providing an automated detection method of the amount of foci and their location in the different strains. *X. citri virB10-msfGFP* wild-type images were used to optimize MicrobeJ parameters for automated detection of the foci. Identical parameters were used for all images and visual inspection was used to confirm detection accuracy. All mutants were imaged and analyzed together and on two separate occasions after which data sets were combined. On average, 2145 cells were analyzed per mutant strain (minimum= 496 cells, maximum= 7329 cells). For quantifiable visualization purposes, a multi-colored lookup table was applied to more easily represent differences in intensity levels and a representative image of *X. citri virB10-msfGFP* is provided in Figure 5a, obtained after a blind deconvolution of the obtained Z-stacks (Leica LAS X software). In Figure 6a (top panel), the number of foci in each cell is represented by the randomly placed shaded circles in each bin (N=0, 1, 2, …9; Tukey box and whisker plots are shown to depict the data: the black central line is the median, the outer end of the whiskers is data within 1.5 IQR, box limits represent first and third quartiles). The images were also used to measure the average total fluorescence intensities of all the mutants using identical software packages as described above for *X. citri virB10-msfGFP* foci detection. This allowed for an independent measure of the VirB10-msfGFP levels and can be compared to the results observed in western blots presented in Figure 6 and Supplementary Figure 7b.

VirB10-msfGFP fusion protein total fluorescence

X. citri virB10-msfGFP and *X. citri* P*virD4-msfGFP* (control strain expressing cytoplasmic msfGFP under regulation of the *virD4* promotor) strains were grown overnight in AB medium (0.2% $(NH_4)_2SO_4$, 0.6% Na_2HPO_4, 0.3% KH_2PO_4, 0.3% NaCl, 0.1 mM $CaCl_2$, 1 mM $MgCl_2$, 3 μM $FeCl_3$) supplemented with 0.2% sucrose, 0.2% casamino acids, 10 μg/mL thiamine and 25 μg/mL uracil, re-inoculated in four volumes of fresh supplemented AB medium and grown for an additional five hours at 28 ºC under agitation. Cells were aliquoted and washed once in 1X buffer A at pH 7.0. After one hour of incubation at 30 ºC, cells were spotted on thin agar slabs and imaged using a Leica DMI-8 epifluorescent microscope. For each image, GFP excitation was recorded at maximum intensity levels with an exposure time of 1500 ms together with phase contrast images. The microscope was equipped with a DFC365 FX camera (Leica), a HC PL APO 100x/1.4 Oil ph3 objective (Leica) and a GFP excitation-emission band-pass filter cube (Ex.: 470/40, DC: 495, Em.: 525/50; Leica). The images were analyzed using the MicrobeJ software package41 and background-corrected total fluorescent intensities of all individual cells were analyzed using RStudio software38 and plotted as box-plots using the ggplot2 package39. On average 1930 cells (minimum=496 cells; maximum=7329 cells) were analyzed at each pH for each strain.

The precise number of cells analyzed for each strain presented in Supplementary Figure 7b is shown in the upper panel of Figure 6a. In the experiments described in Supplementary Figure 7a, cells were resuspended in 1X buffer A adjusted to different specific pH values (5.0, 5.5, 6.0, 6.5, 7.0, 7.5 and 8.0). *X. citri virB10-msfGFP* (wild-type and mutants) and *X. citri* P*virD4-msfGFP* cells at the same pH were measured side by side. One dataset was obtained by starting measurements from cells incubated at pH 5.0 going upwards and a second independent dataset was obtained in the same manner but starting from pH 8.0 and continuing downwards. Both datasets were combined, correcting for putative differences in GFP fluorescent intensities arising from different incubation times (approximately 60 minutes of time difference between first and last sample). In these pH-dependence experiments, an average of 2441 cells (minimum=1059 cells; maximum=4294 cells) were analyzed at each pH for each strain. For the precise number of cells analyzed at each pH value for each strain, please refer to Supplementary Figure 7a.

Western blot assays

To detect *X. citri* core complex proteins (VirB7, VirB9 and VirB10), western blot assays were performed using total protein extract for the wild-type and each mutant strain analyzed. Polyclonal antibodies specific for each protein were used. In addition, the VirB10-msfGFP chimera produced in the *virB10-msfgfp* background was also detected using an anti-GFP antibody. Finally, as a control for the expression and accumulation of the rest of the T4S system in these *X. citri* strains, the levels of VirB8 was also evaluated. *X. citri* cells were grown overnight in AB medium (0.2% $(NH_4)_2SO_4$, 0.6% Na_2HPO_4, 0.3% KH_2PO_4, 0.3% NaCl, 0.1 mM $CaCl_2$, 1 mM $MgCl_2$, 3 μM $FeCl_3$)37 supplemented with 0.2% sucrose, 0.2% casamino acids, 10 μg/mL thiamine and 25 μg/mL uracil. After this, OD_{600} for all strains were measured and adjusted to the same value (OD_{600}=1.3). Cells from 1 mL were collected by centrifugation for 5 minutes at 6,000 x g, resuspended in 500 μL of 1X PBS and 125 μL of denaturing sample buffer and incubated for 5 minutes at 95 ºC. *E. coli* cells expressing *virB7-B8-B9-B10* were used as a control. Samples (20 μL) were resolved in 15-well Tricine-SDS-PAGE gels42, transferred to nitrocellulose membrane (Bio Rad), and blocked for 1 hour using 5% skimmed milk in 1X PBS. Primary antibodies produced in rabbit against VirB7 (AbVirB7; 1:20,000 dilution), VirB8 (AbVirB8; 1:10,000), VirB9 (AbVirB9; 1:4,000), VirB10 (AbVirB10; 1:5,000) and GFP (AbGFP; Sigma-Aldrich G1544; 1:6,000) were used. Secondary goat anti-rabbit IgG-AP conjugate (Bio Rad 1706518; 1:5,000) was used for AbVirB7 and AbVirB8 with BCIP (VWR 0885) and NBT (Sigma-Aldrich N6876) for detection, and secondary goat anti-rabbit IgG-IRDye® 800CW (Li-Cor 32211; 1:8,000) was used for AbVirB9, AbVirB10 and AbGFP prior to visualization using an Odyssey imaging system (Li-Cor).

Supplementary Material

Refer to Web version on PubMed Central for supplementary material.

Acknowledgements

References

1. Alvarez-Martinez CE, Christie PJ. Biological Diversity of Prokaryotic Type IV Secretion Systems. Microbiol Mol Biol Rev. 2009; 73:775–808. [PubMed: 19946141]

2. Odenbreit S. Translocation of Helicobacter pylori CagA into Gastric Epithelial Cells by Type IV Secretion. Science (80-.). 2000; 287:1497–1500.

3. Isaac DT, Isberg R. Master manipulators: an update on Legionella pneumophila Icm/Dot translocated substrates and their host targets. Future Microbiol. 2014; 9:343–359. [PubMed: 24762308]

4. Kotob SI, Hausman SZ, Burns DL. Localization of the promoter for the ptl genes of Bordetella pertussis, which encode proteins essential for secretion of pertussis toxin. Infect Immun. 1995; 63:3227–3230. [PubMed: 7622254]

5. De Jong MF, Tsolis RM. Brucellosis and type IV secretion. Future Microbiology. 2012; 7:47–58. [PubMed: 22191446]

6. Dehio C, Tsolis RM. Type IV effector secretion and subversion of host functions by bartonella and brucella speciesCurrent Topics in Microbiology and Immunology. Vol. 413. Springer; Cham: 2017. 269–295.

7. Siamer S, Dehio C. New insights into the role of Bartonella effector proteins in pathogenesis. Current Opinion in Microbiology. 2015; 23:80–85. [PubMed: 25461577]

8. Souza DP, et al. Bacterial killing via a type IV secretion system. Nat Commun. 2015; 6 6453.

9. Oliveira LC, et al. VirB7 and VirB9 Interactions Are Required for the Assembly and Antibacterial Activity of a Type IV Secretion System. Structure. 2016; 24:1707–1718. [PubMed: 27594685]

10. Chandran V, Waksman G. Structural Biology of Bacterial Type IV Secretion Systems. Annu Rev Biochem. 2015; 84:603–629. [PubMed: 26034891]

11. Low HH, et al. Structure of a type IV secretion system. Nature. 2014; 508:550–553. [PubMed: 24670658]

12. Costa TRD, et al. Secretion systems in Gram-negative bacteria: structural and mechanistic insights. Nat Rev Microbiol. 2015; 13:343–359. [PubMed: 25978706]

13. Trokter M, Felisberto-Rodrigues C, Christie PJ, Waksman G. Recent advances in the structural and molecular biology of type IV secretion systems. Curr Opin Struct Biol. 2014; 27:16–23. [PubMed: 24709394]

14. Fronzes R, et al. Structure of a Type IV Secretion System Core Complex. Science (80-.). 2009; 323:266–268.

15. Chandran V, et al. Structure of the outer membrane complex of a type IV secretion system. Nature. 2009; 462:1011–1015. [PubMed: 19946264]

16. Souza DP, et al. A component of the Xanthomonadaceae type IV secretion system combines a VirB7 motif with a N0 domain found in outer membrane transport proteins. PLoS Pathog. 2011; 7:e1002031. [PubMed: 21589901]

17. Rivera-Calzada A, et al. Structure of a bacterial type IV secretion core complex at subnanometre resolution. EMBO J. 2013; 32:1195–1204. [PubMed: 23511972]

18. Gordon JE, et al. Use of chimeric type IV secretion systems to define contributions of outer membrane subassemblies for contact-dependent translocation. Mol Microbiol. 2017; 105:273–293. [PubMed: 28452085]

19. Zheng SQ, et al. MotionCor2: anisotropic correction of beam-induced motion for improved cryo-electron microscopy. Nat Methods. 2017; 14:331–332. [PubMed: 28250466]

20. Zhang K. Gctf: Real-time CTF determination and correction. J Struct Biol. 2016; 193:1–12. [PubMed: 26592709]

21. Scheres SHW. RELION: Implementation of a Bayesian approach to cryo-EM structure determination. J Struct Biol. 2012; 180:519–530. [PubMed: 23000701]

22. Punjani A, Rubinstein JL, Fleet DJ, Brubaker MA. CryoSPARC: Algorithms for rapid unsupervised cryo-EM structure determination. Nat Methods. 2017; 14:290–296. [PubMed: 28165473]

23. Pettersen EF, et al. UCSF Chimera - A visualization system for exploratory research and analysis. J Comput Chem. 2004; 25:1605–1612. [PubMed: 15264254]

24. Emsley P, Lohkamp B, Scott WG, Cowtan K. Features and development of Coot. Acta Crystallogr Sect D Biol Crystallogr. 2010; 66:486–501. [PubMed: 20383002]

25. Adams PD, et al. PHENIX: A comprehensive Python-based system for macromolecular structure solution. Acta Crystallogr Sect D Biol Crystallogr. 2010; 66:213–221. [PubMed: 20124702]

26. Chen VB, et al. MolProbity: All-atom structure validation for macromolecular crystallography. Acta Crystallogr Sect D Biol Crystallogr. 2010; 66:12–21. [PubMed: 20057044]

27. The PyMOL Molecular Graphics System v.1.8. Schrödinger, LLC;

28. Cavanagh J, Fairbrother WJ, Palmer AG, Rance M, Skelton NJ. Protein NMR spectroscopy : principles and practice. Academic Press; 2007.

29. Delaglio F, et al. NMRPipe: A multidimensional spectral processing system based on UNIX pipes. J Biomol NMR. 1995; 6:277–293. [PubMed: 8520220]

30. Vranken WF, et al. The CCPN data model for NMR spectroscopy: Development of a software pipeline. Proteins Struct Funct Genet. 2005; 59:687–696. [PubMed: 15815974]

31. Marsh JA, Singh VK, Jia Z, Forman-Kay JD. Sensitivity of secondary structure propensities to sequence differences between α- and γ-synuclein: Implications for fibrillation. Protein Sci. 2006; 15:2795–2804. [PubMed: 17088319]

32. Shen Y, Bax A. Protein backbone and sidechain torsion angles predicted from NMR chemical shifts using artificial neural networks. J Biomol NMR. 2013; 56:227–241. [PubMed: 23728592]

33. Ke N, Landgraf D, Paulsson J, Berkmen M. Visualization of periplasmic and cytoplasmic proteins with a self-labeling protein tag. J Bacteriol. 2016; 198:1035–1043. [PubMed: 26787765]

34. da Silva ACR, et al. Comparison of the genomes of two Xanthomonas pathogens with differing host specificities. Nature. 2002; 417:459–463. [PubMed: 12024217]

35. Sawitzke JA, et al. Probing cellular processes with oligo-mediated recombination and using the knowledge gained to optimize recombineering. J Mol Biol. 2011; 407:45–59. [PubMed: 21256136]

36. Vettiger A, Basler M. Type VI Secretion System Substrates Are Transferred and Reused among Sister Cells. Cell. 2016; 167:99–110.e12. [PubMed: 27616061]

37. Clark DJ, Maaloe O. DNA replication and the division cycle in Escherichia coli. J Mol Biol. 1967; 23:99–112.

38. RStudio Team. RStudio: Integrated Development for R. 2016

39. Wickham H. ggplot2. Springer-Verlag; New York: 2009.

40. Schindelin J, et al. Fiji: an open-source platform for biological-image analysis. Nat Methods. 2013; 9:676–682.

41. Jiang C, Brown PJB, Ducret A, Brun YV. Sequential evolution of bacterial morphology by co-option of a developmental regulator. Nature. 2014; 506:489–493. [PubMed: 24463524]

42. Schägger H. Tricine-SDS-PAGE. Nat Protoc. 2006; 1:16–22. [PubMed: 17406207]

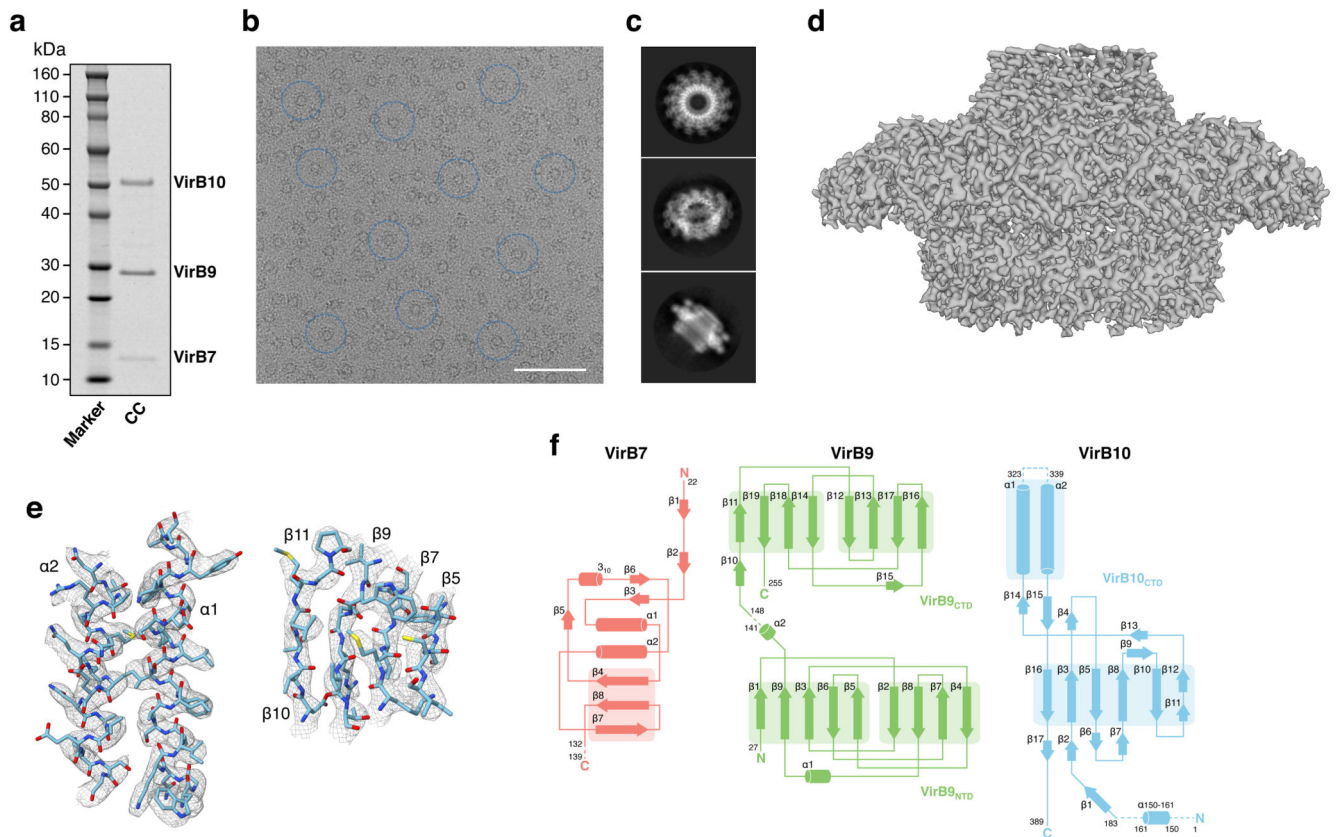**Figure 1. Biochemistry and electron microscopy map and model of the *X. citri* T4S system core complex.**

a, SDS-PAGE of the VirB7-VirB9-VirB10 core complex. Left lane labeled "Marker": molecular weight markers, with the molecular weight for each band shown at left. Right lane labeled "CC": purified core complex, with the three components labeled at right. Purification assays were repeated more than ten times with similar results (see also Supplementary Figure 9a). **b**, Electron micrograph of the *X. citri* core complex, with some particles highlighted in blue circles. Scale bar: 50 nm. Experiments were repeated at least 8 times showing similar results. **c**, Representative of top, tilt, and side view 2D class averages obtained using RELION 2.0 (see the Methods section for more information). **d**, Overview of the 3.3-Å electron density, contoured at 4 σ level. **e**, Two representative regions of the electron density of the *X. citri* core complex. Electron density map contoured at a 4 σ level is shown in chicken wire representation, color-coded in grey-blue. The final model built into the map is shown in a ribbon and stick representation color-coded dark blue, red, yellow, and light blue for nitrogen, oxygen, sulfur and carbon atoms, respectively. Secondary structures are labeled. The regions depicted are both from the VirB10$_{CTD}$ (left panel for α-helices and right panel for β-strands). **f**, Topology secondary structure diagrams of VirB7 (red), VirB9 (green), and VirB10 (blue). β-strands and α-helices are represented as arrows and cylinders, respectively. Regions for which no electron density was observed are indicated by dashed lines. Note that the 182 N-terminal residues of VirB10 were disordered and could not be traced except for a small helix corresponding to residues 150-161. This is not unexpected considering that the 101 amino acid stretch (residues 84-184) between the inner membrane

spanning helix and the globular VirB10$_{CTD}$ is rich in proline residues (Supplementary Fig. 2).
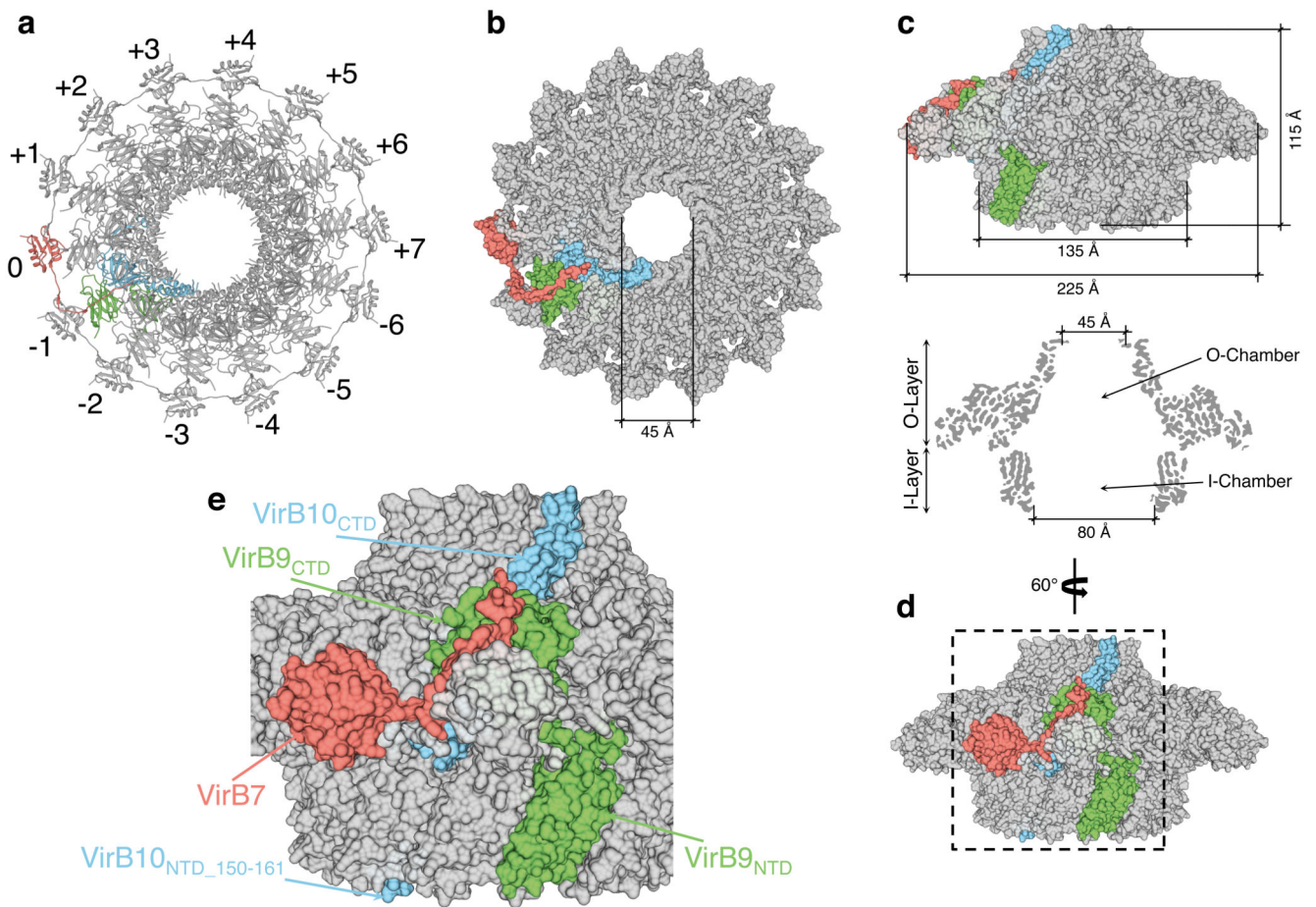
Figure 2. Structure of the *X. citri* T4S system core complex.
a, Top view of the structure in ribbon representation with one VirB7-VirB9-VirB10 heterotrimer shown in red, green and blue, respectively (coloring maintained in parts **b**-**e**). The heterotrimer numbering used in this study is indicated, with the colored heterotrimer serving as reference and therefore numbered 0. **b** and **c**, Top view (**b**) and side view (**c, upper panel**) of the structure in surface representation. **c, lower panel**: cut-away side view of the model. External and internal dimensions of specific structural features are indicated in **b** and **c**. The 80-Å opening at the bottom of the I-chamber is similar to that observed for the 8.5-Å cryo-EM structure of the elastase-digested pKM101 core complex17. **d** and **e**, Side view of the structure in surface representation as in **c** but rotated 60 degrees counter-clockwise to show heterotrimer 0 more clearly. **e** is a zoomed in view of the region delimited by the dashed line in **d**.
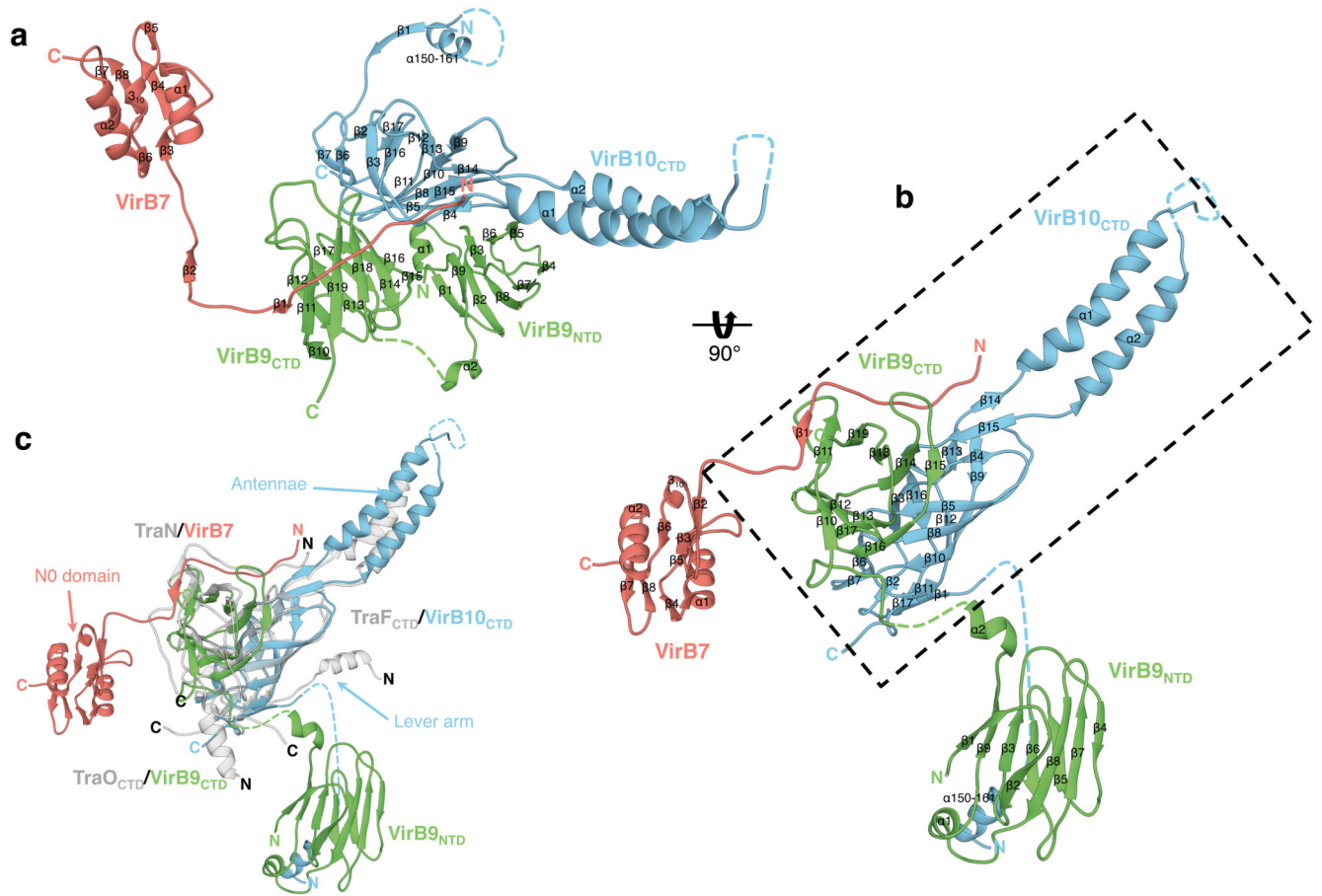
Figure 3. The heterotrimer of the *X. citri* T4S system core complex structure and comparison with that of pKM101 from *E. coli*.

The *X. citri* VirB7-VirB9-VirB10 heterotrimer. **a**, Proteins are shown in ribbon representation and color-coded as in Figure 2. Specific domains are labeled, as also are the secondary structures in each protein. The linkers between VirB9 NTD and CTD, the two α-helices of the VirB10 "antennae" and the CTD of VirB10 and $VirB10_{NTD\_150-161}$ helix are shown in dashed green and blue lines, respectively, as they are disordered in the structure. The orientation is as in Figure 2a. **b**, Same as in **a**, but rotated 90 degrees to correspond to the side view shown in Figure 2c. The box delimits the central compact core. **c**, Superposition of the structure of the *X. citri* heterotrimer (in red, green and blue) with that of the pKM101 complex (grey) composed of TraN/VirB7, $TraO_{CTD}/VirB9_{CTD}$, and $TraF_{CTD}/VirB10_{CTD}$.
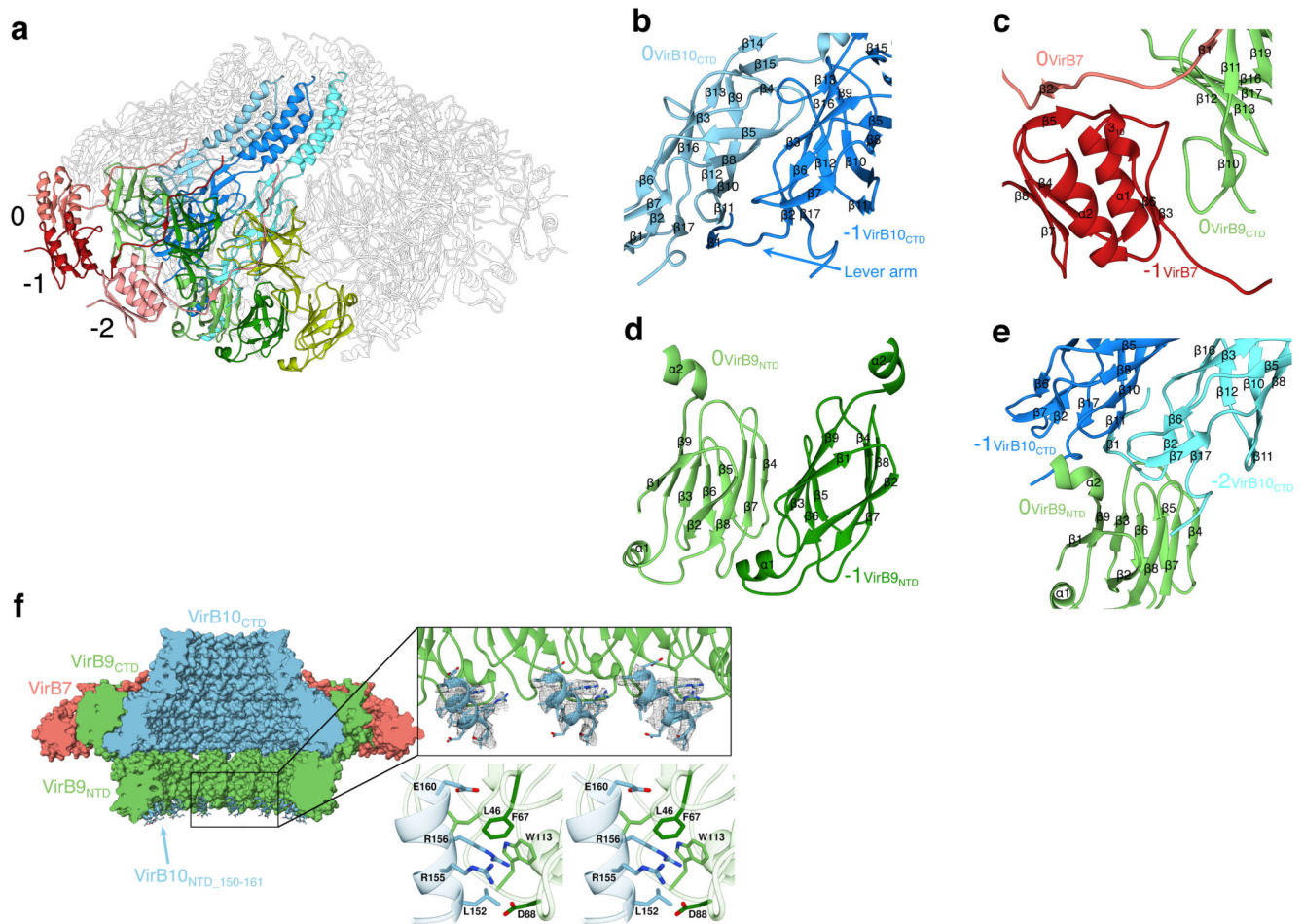
Figure 4. Interactions between heterotrimers in the *X. citri* T4S system core complex.
a, Overall structure of the core complex with 3 heterotrimers highlighted. These are labeled 0, -1, and -2 and color-coded as in Figure 2 with different shades of the respective colors for each heterotrimer. **b**, Interactions between the VirB10$_{CTD}$s of heterotrimer 0 (0VirB10$_{CTD}$) and -1 (-1VirB10$_{CTD}$). The β1 strand is labeled "Lever arm" due to its correspondence to part of the same structural feature observed in pKM101 core complex O-layer[15]. **c**, Interactions between the VirB9$_{CTD}$ of heterotrimer 0 (0VirB9$_{CTD}$) and VirB7 of heterotrimer 0 (0VirB7) and -1 (-1VirB7). **d**, Interactions between adjacent VirB9$_{NTD}$s. The two VirB9$_{NTD}$s shown are from heterotrimer 0 (0VirB9$_{NTD}$) and -1 (-1VirB9$_{NTD}$). **e**, Interactions between the VirB9$_{NTD}$ of heterotrimer 0 (0VirB9$_{NTD}$) and VirB10$_{CTD}$ of heterotrimer -1 (-1VirB10$_{CTD}$) and -2 (-2VirB10$_{CTD}$). **f**, Interactions of a helical structure belonging to VirB10$_{NTD}$ (VirB10$_{NTD\_150-161}$) with two adjacent VirB9$_{NTD}$s. Left panel: surface representation of the lumen of the *X. citri* core complex structure, color-coded by proteins with VirB7, VirB9, and VirB10 in red, green and blue, respectively. Upper-right panel: zoomed view of the region contained in the black box shown at left. VirB9$_{NTD}$s and the VirB10$_{NTD\_150-161}$ helix are shown in ribbon representation. The electron density for the VirB10$_{NTD\_150-161}$ is also shown (grey) contoured at 4 σ level. Lower-right panel: stereo figure of residue specific interactions between the VirB10$_{NTD\_150-161}$ helix and two adjacent

VirB9$_{NTD}$s. The side chains of interfacing residues are in stick representation with nitrogen and oxygen atoms colored in blue and red, respectively. Carbon atoms are in the color of the ribbon they emanate from. Two shades of green were used to distinguish residues from two different VirB9 chains.
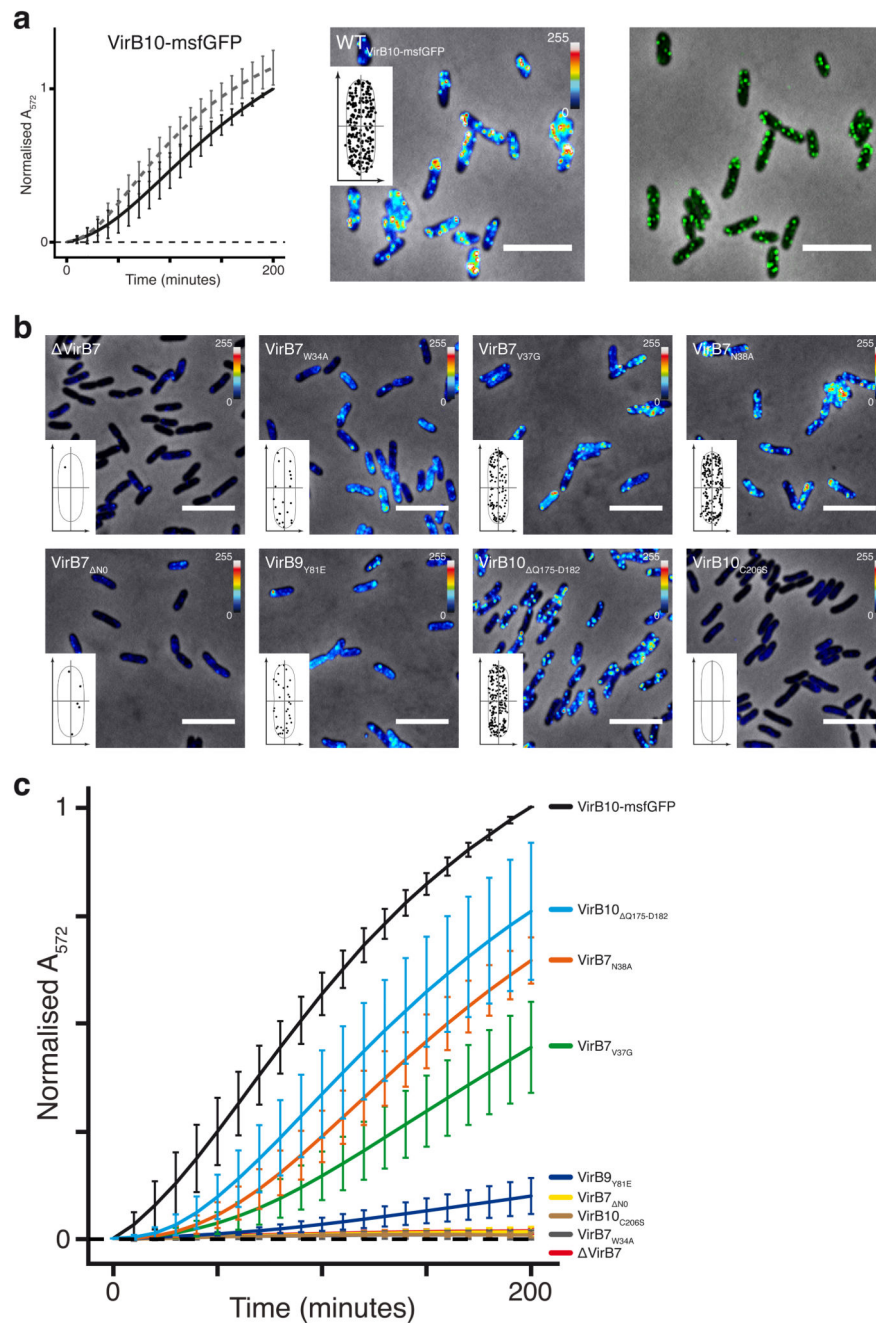
Figure 5. Effect of specific mutations in the core complex on T4S system-mediated cell lysis of neighboring *E. coli* cells and VirB10 localization.

a, Left panel: Bacterial killing assay measuring the ability of *X. citri* to use the T4S system to lyse neighboring *E. coli* cells. The results obtained for wild-type *X. citri* cells (dashed grey line) are compared to the assay performed using the *X. citri virB10-msfGFP* strain (solid black line). The dashed black horizontal line corresponds to the no lysis baseline after subtracting the *E. coli* only background signal from the data. Data are mean ± s.d. (n=9 for *X. citri virB10-msfGFP* and n=27 for wild-type *X. citri*). Central panel: Representative

image of the *X. citri virB10-msfGFP* strain as obtained by epifluorescence microscopy displaying discrete msfGFP foci that indicate the presence of T4S systems. Image shows msfGFP intensity levels of a 0.5-μm region containing the focal plane of the cells. The inset shows the superposition of the locations of fluorescent VirB10-msfGFP foci obtained from 100 individual *X. citri virB10-msfGFP* cells. Right panel: An enhanced image obtained by deconvolution of the obtained Z-slices (not used for quantification) more clearly showing discrete foci (see Methods). Scale bar: 5 μm. The *X. citri virB10-msfGFP* strain was imaged and analyzed at least 6 times independently with similar results. **b**, Representative epifluorescence microscopy images (as described in **a**) for a selected series of *X. citri virB10-msfGFP* mutant strains in VirB7, VirB9 or VirB10. Note that VirB7 and VirB10$_{C206S}$ cells are mostly devoid of fluorescence. Other strains, such as VirB7$_{W34A}$, present more diffuse fluorescence and lack clear foci. Also note that the few foci shown in the cell contour insets of mutants severely deficient in killing (see below) are due to occasional background detection. Scale bar: 5 μm. All *X. citri virB10-msfGFP* mutant strains were imaged and analyzed together on two separate occasions independently with similar results. **c**, Bacterial killing assays of the *X. citri virB10-msfGFP* strains shown in **b**. Each *X. citri virB10-msfGFP* mutant was compared to the *X. citri virB10-msfGFP* strain (solid black line). Data are mean ± s.d. (n=9 for *X. citri virB10-msfGFP* and n=4 for each mutant).
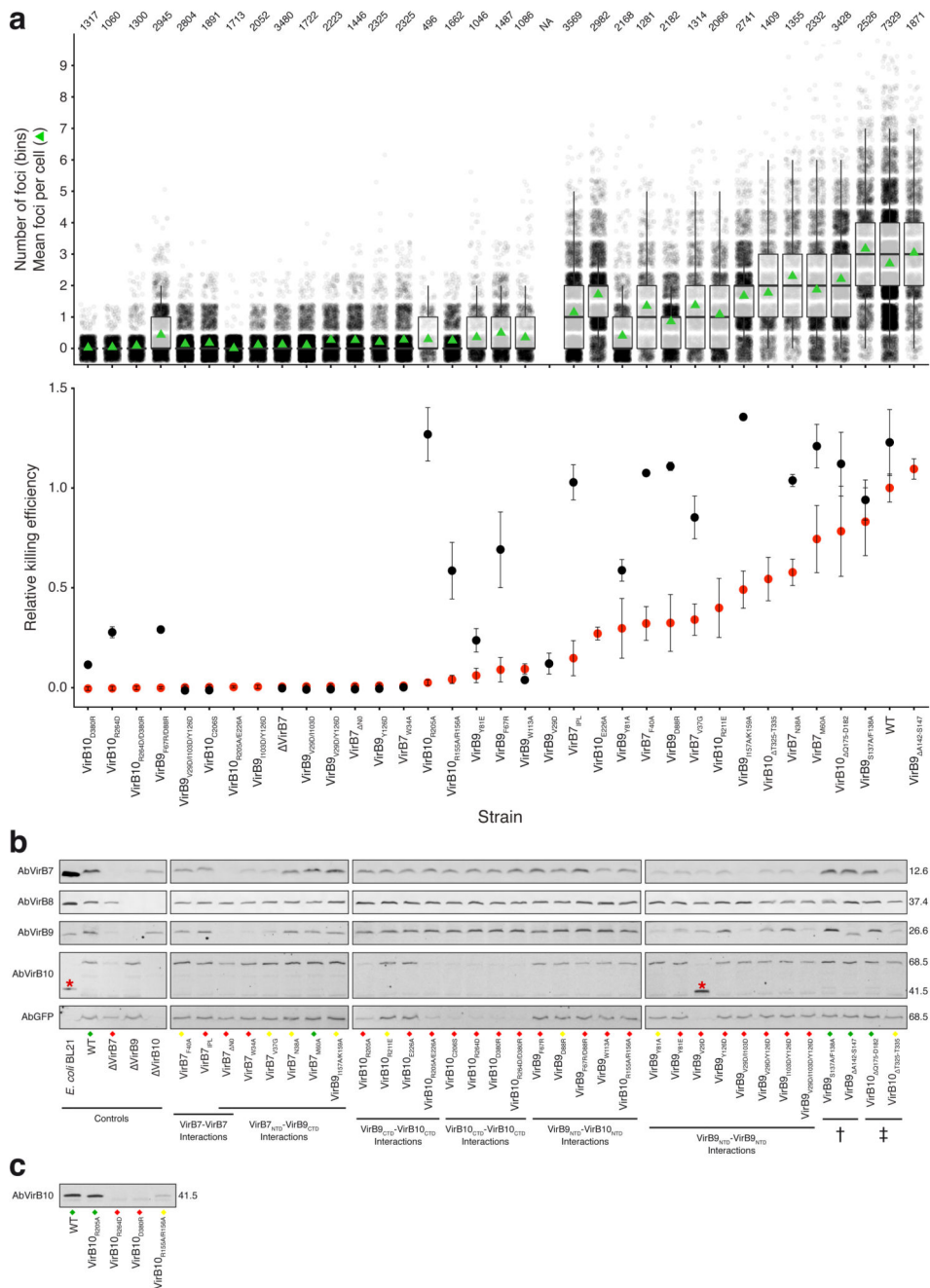
Figure 6. Killing efficiency is correlated with T4S system assembly in *X. citri*.
a, Top panel: The relative number of VirB10-msfGFP foci per cell is plotted for each strain. The distribution of cells according to the number of foci per cell is represented by the randomly placed shaded circles in each bin. Tukey box and whisker plots depict the data: black central line (median), box (first and third quartiles), whiskers (data within 1.5 IQR), green triangles (mean) (see Supplementary Table 4). The sample size (n) of cells of each strain analyzed by fluorescence microscopy (from two independent experiments) is listed at the top. Bottom panel: The mean (± s.d.) relative capacity of each mutant to lyse *E. coli* cells

in a *X. citri*/*E. coli* co-culture is shown (as in Figure 5 and Supplementary Table 4). Red dots represent mutants produced in the VirB10-msfGFP background and black dots represent mutants produced in the non-GFP background. In competitions using GFP background strains the n=4 (except for VirB9$_{A142-S147}$ (n=3), VirB10$_{T325-T335}$ (n=3),   VirB7 (n=6), and VirB10-msfGFP (n=9). In competitions using non-GFP background strains the n=3. **b**, Western blot assays using polyclonal antibodies (Ab) against specific T4S system components or against msfGFP in different *X. citri virB10-msfGFP* mutant strains (see Methods). The first lane contains total protein extract from *E. coli* BL21(DE3) expressing the *X. citri* core complex with normal length VirB10 as does that for the VirB9$_{V29D}$ mutant (red asterisks), which was obtained only in non-GFP genomic background. Experiments were repeated 3 times with similar results. † indicates mutations in the VirB9 Linker and ‡ indicates mutations in the VirB10 linker for VirB10 $_{Q175-D182}$ or the VirB10 antenna for VirB10 $_{T325-T335}$. Colored diamonds denote the values of the relative killing efficiency according to the code: Less than 0.3 (red), 0.3 to 0.7 (yellow), greater than 0.7 (green) (see **a** and Supplementary Table 4). WT=wild-type. Theoretical molecular weight (in kDa) for each mature protein is shown at right. **c**, Western blot detection of VirB10 in mutant strains produced in the non-GFP genomic background. Annotations are the same as in **b**. Experiments were repeated twice with similar results. Full western blots are presented in Supplementary Figure 9b-g.